

Elemental gas-phase abundances of intermediate redshift type Ia supernova star-forming host galaxies

M.E. Moreno-Raya¹, L. Galbany^{2*}, Á.R. López-Sánchez^{3,4}, M. Mollá⁵,
S. González-Gaitán⁶, J.M. Vílchez⁷, A. Carnero^{8,9}

¹Centro Astronómico Hispano-Alemán(CSIC-MPG), Observatorio Astronómico de Calar Alto, Sierra de los Filabres, E-04550 Gérgal, Almería, Spain

²PITT PACC, Department of Physics and Astronomy, University of Pittsburgh, Pittsburgh, PA 15260, USA

³Australian Astronomical Observatory, 105 Delhi Rd, North Ryde, NSW 2113, Australia

⁴Department of Physics and Astronomy, Macquarie University, NSW 2109, Australia

⁵Departamento de Investigación Básica, CIEMAT, Avda. Complutense 40, 28040, Madrid, Spain

⁶CENTRA, Instituto Superior Técnico, Universidade de Lisboa, Portugal

⁷Instituto de Astrofísica de Andalucía-CSIC, Apdo. 3004, 18008, Granada, Spain

⁸Laboratório Interinstitucional de e-Astronomia - LIneA, Rua Gal. José Cristino 77, Rio de Janeiro, RJ 20921-400, Brazil

⁹Observatório Nacional, Rua Gal. José Cristino 77, Rio de Janeiro, RJ 20921-400, Brazil

Received date: 6 November 2018; accepted date: ***

ABSTRACT

The maximum luminosity of type Ia supernovae (SNe Ia) depends on the oxygen abundance of the regions of the host galaxies where they explode. This metallicity dependence reduces the dispersion in the *Hubble diagram* (HD) when included with the traditional two-parameter calibration of SN Ia light-curve (LC) parameters and absolute magnitude. In this work, we use empirical calibrations to carefully estimate the oxygen abundance of galaxies hosting SNe Ia from the SDSS-II/SNe Survey at intermediate redshift, by measuring their emission line intensities. We also derive electronic temperature with the direct method for a small fraction of objects for consistency. We find a trend of decreasing oxygen abundance with increasing redshift for the most massive galaxies. Moreover, we study the dependence of the HD residuals (HR) with galaxy oxygen abundance obtaining a correlation in line with those found in other works. In particular, the HR vs oxygen abundance shows a slope of $-0.186 \pm 0.123 \text{ mag dex}^{-1}$ (1.52σ), in good agreement with theoretical expectations. This implies smaller distance moduli after corrections for SNe Ia in metal-rich galaxies. Based on our previous results on local SNe Ia, we propose this dependence to be due to the lower luminosity of the SNe Ia produced in more metal-rich environments.

Key words: galaxies: abundances, supernovae, SN Ia, ISM: abundances, H II regions, methods: data analysis, techniques: spectroscopic

1 INTRODUCTION

Type Ia supernovae (SNe Ia) are thermonuclear explosions of carbon-oxygen white dwarfs (WD) in binary systems. In the traditional picture, the WD progenitor increases its mass due to accretion from the companion star until reaching the Chandrasekhar mass limit ($\sim 1.44 M_{\odot}$) when the degenerate electron pressure no longer supports its weight. However, there is evidence that question this picture from several aspects: the exact nature of the companion star (another WD or a main sequence star), the actual mass of the progenitor before explosion (sub- or super- Chandrasekhar), or the

exact explosion mechanism (deflagration or detonation) is still under debate (see e.g. Maoz, Mannucci & Nelemans 2014; Nomoto, Kobayashi & Tominaga 2013). Anyway, since all explosions in principle occur from WD with similar (although not exact) conditions, it is expected that SNe Ia show similar luminosities.

SN Ia light-curves can be *standardized* by empirical correlations between SNe Ia peak brightness and their light-curve (LC) width (Phillips 1993; Phillips et al. 1999) and colour (Riess, Press & Kirshner 1996). Several empirical techniques (Barris & Tonry 2004; Guy et al. 2005; Prieto, Rest & Suntzeff 2006; Jha, Riess & Kirshner 2007; Guy et al. 2007; Burns et al. 2011) have exploited these correlations and found standard absolute peak magnitudes with a dis-

* E-mail: lgalbany@pitt.edu

persion of 0.10-0.15 mag, which corresponds to a precision of 5-7% in the determination of distances (Betoule et al. 2014; Scolnic et al. 2017). Both the quantity and quality of supernova observations have increased, and limitations on the homogeneity of SNe Ia have become apparent (Riess, Press & Kirshner 1996; Sullivan et al. 2006). If these inhomogeneities are not accounted for by LC width and color corrections, these variations may introduce systematic errors in the determination of cosmological parameters, preventing reducing further the uncertainties.

One plausible source of inhomogeneity is the dependence of supernova properties on host galaxy characteristics after other LC corrections. The average properties of host galaxies evolve with redshift, thus any such dependence not included in the standardization techniques will have an effect on the cosmological parameter determination. During the last decade, there have been many studies illustrating the dependence of SNe Ia light-curve parameters on global characteristics of their hosts (Sullivan et al. 2006; Gallagher et al. 2008; Howell et al. 2009; Hicken et al. 2009; Kelly et al. 2010; Sullivan et al. 2010; Lampeitl et al. 2010; D’Andrea et al. 2011; Gupta et al. 2011; Nordin et al. 2011; Sullivan et al. 2011; Galbany et al. 2012; Johansson et al. 2013). Some of these latter studies found additionally that SNe Ia are systematically brighter in massive host galaxies **after LC shape and color corrections**. Through the mass-metallicity relation Tremonti et al. (2004), this would lead to a correlation between SN Ia brightness and the metallicity of their host galaxies: metal-richer galaxies host brighter SNe Ia **after corrections** with a difference of ~ 0.10 mag, the same order of magnitude of the uncertainties in the standard absolute magnitude. However, the cause of these correlations is not well understood.

In fact, a dependence of the SN Ia peak luminosity with metallicity of the binary system was theoretically predicted: assuming that the mass of the progenitor WD at explosion is fixed, the SN Ia peak magnitude depends mainly on the total quantity of ^{56}Ni , synthesized during the explosion. Timmes, Brown & Truran (2003) showed that the magnitude in the LC maximum depends on the WD progenitor chemical abundance of elements C, N, O and ^{56}Fe : a difference of a factor of 3 in the metallicity may vary the mass of ^{56}Ni ejected during the explosion in a 25%. More recently, Kasen, Röpke & Woosley (2009) analyzed explosion models where asymmetries were taken into account and they found a weak dependence of the SN Ia luminosity on abundances as C and O, claiming that without correcting for this effect, the cosmological distances of these objects may be overestimated by a 2%. Bravo et al. (2010) also modeled a series of explosions of SNe Ia finding a non-linear relation between the synthesized mass $M(^{56}\text{Ni})$ and the metallicity Z of the progenitor binary system (see their Fig.1), stronger than the previous results. Summarizing, the luminosity of SNe Ia may depend crucially on the abundance of elements within the progenitor system, being brighter when Z is lower than for solar abundances.

Taking all these into account, we have carried out an observational project to further investigate the existence and extent of this relationship. Our final aim is to perform a systematic and careful study of the possible metallicity dependence of the luminosity of SNe Ia, and to analyze if the dispersion in the distance modulus is reduced when this pa-

rameter is taken into account. In order to reach our objective, we planned to determine the metallicity of the SN Ia progenitor systems using the oxygen abundance of the host galaxies. To do that, we have divided our study in three parts, corresponding to three redshift ranges:

- (i) The local Universe, $z < 0.03$, whose results have been presented in Moreno-Raya et al. (2016a,b, hereafter Paper I and Paper II, respectively).
- (ii) The intermediate redshift range, $0.03 < z < 0.5$, for which we analyze a sample of ~ 400 SN Ia host galaxies estimating their metallicities and investigating their dependence on SN Ia LC parameters. The present work is devoted to this part of the project.
- (iii) Finally, the high redshift range, $z > 0.5$, where cosmological models diverge. This will be presented in a future work.

In Paper I and Paper II, we have presented long-slit spectroscopy of 28 SN Ia host galaxies in the local Universe ($z < 0.03$) for which distances had been previously derived using methods independent of SNe Ia. We estimated the gas-phase oxygen abundance in the region where each SN Ia exploded from the emission lines observed in their optical spectra. We have demonstrated that there is a correlation between SN Ia absolute magnitudes and oxygen abundances at the explosion sites, in the sense that SNe Ia tend to be brighter at metal-poorer locations. This relation may explain why after standardizing SN Ia luminosities, brighter SNe Ia are usually found in metal-richer or more massive galaxies, implying that the standard calibration tends to overestimate the luminosities of these objects. In this way, if the metallicity dependence is neglected, the standardized luminosity of a SN Ia in a metal-rich environment would be higher than the actual value, thus showing a residual to the best cosmology of the same order than actually observed. Furthermore, we estimated from our local sample that when this oxygen abundance dependence is included, the dispersion in M_B is reduced by $\sim 5\%$.

In this work we will concentrate on point (ii) estimate oxygen abundances for a sample of intermediate redshift SN Ia host galaxies. Campbell, Fraser & Gilmore (2016) presented a systematic study of the relationships between the SNe Ia properties and the host galaxies characteristics for a sample of 581 SNe Ia from the SDSS-II SN survey, which covers a redshift range of $0.05 < z < 0.55$. They find a slight correlation between HR and host galaxy metallicity, and also a stronger correlation with the host galaxy stellar mass. Moreover, they studied possible effects of these dependences on cosmological parameters, allowing a new free parameter in the fit of data to the models in the HD, resulting in a shift over the parameter w of the equation of state towards a more negative value, $w \sim -1.15^{+0.123}_{-0.121}$, compared with the value of $w \sim -0.970$ obtained without any dependence on mass or metallicity (a 18% of difference). An important caveat of this work is that they also use data from passive galaxies, for which there are no emission lines with sufficient S/N, obtaining however some upper limits from the continuum flux in the regions where the lines are expected. In this way they obtain two different zones in the HR as a function of oxygen, where these upper limit abundances showing values larger than $12 + \log(O/H) > 8.8 - 8.9$ dex, may not be considered valid. Even so, they find a correlation

with a slope $-0.155 \text{ mag dex}^{-1}$, that implies a difference of $\sim 0.150 \text{ mag}$ between objects with $12 + \log(O/H) = 8.0 \text{ dex}$ and 9.0 dex , the most metal rich, after LC shape and color correction, being brighter. In addition, the emission lines used in that work are not directly measured but taken from tables in Thomas et al. (2013). Due to the high number of spectra, these line intensities were obtained by automatic methods which are not always precise enough as already shown in Wolf et al. (2016), who instead measured their own intensities, optimizing the method to subtract the continuum component, for which they needed to reduce the redshift range to $z < 0.3$. They measured H_α and $[\text{NII}]$ simultaneously, fixing the velocity, too. Thus, they improve the measurements of the emission lines despite the reduction of redshift range, and, in consequence, the number of objects to 144.

In this work we estimate the oxygen abundances for a sample of intermediate redshift SN Ia host galaxies. Our final aim is to check if the SNe luminosities maintain the dependence on oxygen abundances as we found previously in the local Universe, and if the HR dependence on metallicity vanishes when a new parameter γ is considered. We carefully measured all the emission lines determining the stellar continuum and the Balmer absorption when possible. The selection of the host galaxy sample is presented in Section 2. The analysis of the galaxy spectra and the determination of oxygen abundances is detailed in Section 3, where the estimation of oxygen abundances from intensity ratios by the different empirical calibration methods is discussed, In Section 4 we discuss our results, and our conclusions are given in Section 5.

2 SAMPLE SELECTION

2.1 The SDSS-II Supernova Survey

The Sloan Digital Sky Survey-II Supernova Survey (SDSS-II/SNe) (Frieman et al. 2008) has identified and measured LCs for intermediate redshift ($0.01 < z < 0.45$) SNe Ia during the three fall seasons of operation from 2005 to 2007, using the dedicated SDSS 2.5m telescope at Apache Point Observatory (Gunn et al. 1998, 2006). These SNe are all located in Stripe 82, a 2.5 degree wide region along the Celestial Equator from roughly $-50 < RA < 59$ in the Southern Galactic hemisphere (Stoughton et al. 2002). This effort resulted in 536 SNe Ia confirmed spectroscopically (sp-Ia), and 914 transients photometrically classified as SNe Ia (ph-Ia) from their LCs (Sako et al. 2014) and using the spectroscopic redshift of the host galaxy either measured previously by the SDSS Legacy Survey (York et al. 2000) or by the BOSS Survey (Dawson et al. 2013). In addition, we add to this sample 16 SNe Ia from the pilot SDSS-II/SNe survey performed in 2004, doing a total of 1466 host SNe Ia galaxies. We finally select those galaxies with optical spectra publicly available in the SDSS Data Release 12 (DR12, Alam et al. 2015). From the initial set of 1466 galaxies, 1128 (344 sp-Ia and 784 ph-Ia) pass the above criterion.

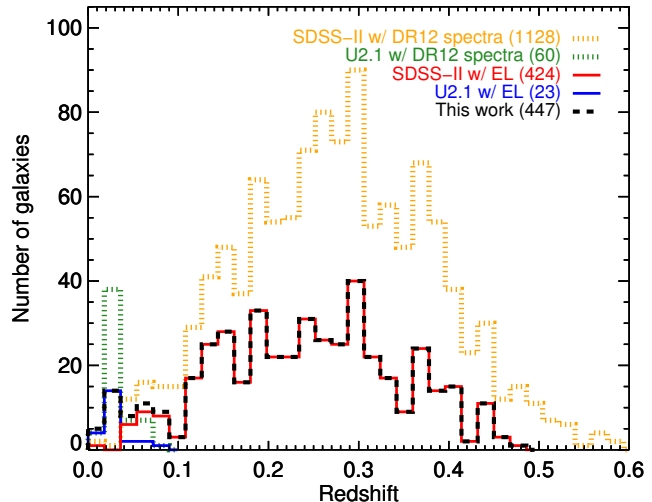


Figure 1. Histogram showing redshift distribution of our spectroscopic sample of SNe Ia host galaxies from SDSS DR12. In red (SDSS) and blue (Union 2.1) our analyzed sample extend above all redshifts. In green the initial complete sample (60) of Union2.1 with spectra, and in orange, the 1128 SDSS SNe Ia hosts galaxies with spectra. The black dashed line denotes the final distribution of 447 objects from both sources used in this work.

2.2 The Union2.1 compilation

We repeat the procedure with the SNe in the Union 2.1 compilation (Suzuki et al. 2012), which contains SNe Ia from several previous works with good quality light-curves and available data to use them for cosmological purposes. From the initial set of 580 SNe Ia, we find 60 with their host galaxy spectra publicly available in SDSS DR12. These 60 SNe are at the lowest redshift range of the Union2.1 (hereafter U2.1) compilation, between 0.015 and 0.17, with 20 of them (a 30%) with $z < 0.05$. The original publication sources are described in Suzuki et al. (2012).

2.3 Host galaxy spectroscopic sample

The spectral SN Ia host galaxy sample we use in this work consists, therefore, of 1188 objects: 1128 from the SDSS-II/SNe survey and 60 from the Union 2.1 compilation. The corresponding spectra present different qualities, depending on the presence of sky lines, the SNR ratio or faintness of the lines. In the next section, we detail the analysis performed with these spectra. The wavelength range in the observer frame covers from 3700 to 9000Å so this permits to measure the needed emission lines up to redshift 0.45, where H_α and $[\text{NII}] \lambda 6583$ are located at 9545Å.

Spectra were obtained with a 2" or 3" diameter fiber¹ pointed to the center of each galaxy, so the light captured by the fiber corresponds to different fractions of the galaxy depending on the galaxy projected size in the sky and the redshift. This may imply a difference between the real metallicity in the zone where SNe Ia exploded and the one estimated which will correspond to different fractions of the

¹ While SDSS-I and SDSS-II spectra were observed with a fiber with 3" diameter, BOSS spectra were observed with a 2" diameter fiber.

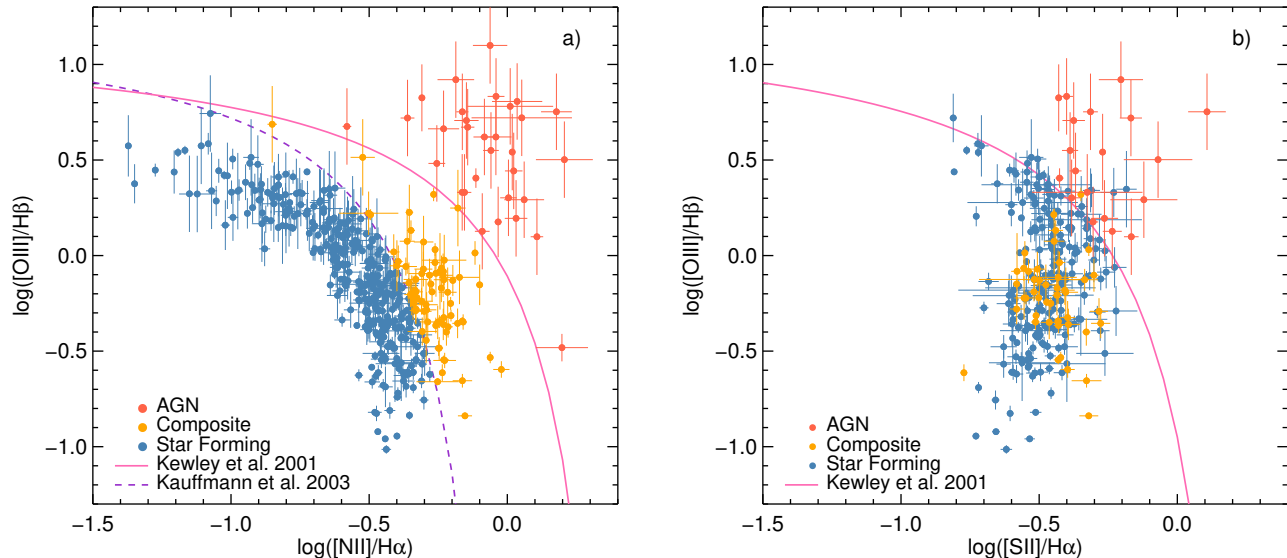


Figure 2. Diagnostic diagrams. Left) Observational flux ratios, $[O\text{ III}]\lambda 5007/H\beta$ vs $[N\text{ II}]\lambda 6583/H\alpha$, obtained analyzing our galaxy sample. The theoretical line derived by Kewley et al. (2001) that divides the emission between ionization from massive stars and AGNs is shown in pink. In a purple dashed line we show the empirical line from Kauffmann et al. (2003) that divides further the space between pure star-forming and composite regions. Blue circles indicate pure star-forming galaxies, yellow points are the galaxies with composite nature, while galaxies classified as AGN are represented in red. Right) $[O\text{ III}]\lambda 5007/H\beta$ vs $[S\text{ II}]\lambda 6716/H\alpha$, with a similar Kewley et al. (2001)’s line dividing AGNs from composite and star forming objects.

galaxy (Galbany et al. 2016b), as a consequence of the metallicity radial gradients usually shown in galaxies (Henry & Worthey 1999; Mollá & Díaz 2005), but we have not corrected for this effect. A detailed study of aperture effects on using fiber spectra in SN Ia cosmology will be presented elsewhere (Galbany et al. in prep.).

In Figure 1 we show the distribution in redshift for the sample: In light and dark grey are the complete sample we use for SDSS and Union2.1, respectively. In red (SDSS) and purple (Union2.1), we show the subsample for which we measure emission lines with the adequate signal-to-noise (see next Section).

3 ANALYSIS OF THE HOST GALAXY SPECTRA

3.1 Line measurement and nature of the emission

First, we correct all spectra for Milky Way dust extinction using the dust maps of Schlafly & Finkbeiner (2011) retrieved from the NASA/IPAC Infrared Science Archive (IRSA), applying the standard Galactic reddening law with $R_V = 3.1$ (Cardelli, Clayton & Mathis 1989; O’Donnell 1994). We also shift the spectra to the rest frame wavelengths.

In these 1188 spectra we try to measure seven emission lines: three hydrogen Balmer lines ($H\alpha$, $H\beta$, $H\gamma$) and the brightest collisional excited lines of heavy elements: $[O\text{ II}]\lambda\lambda 3726, 29$ (blended), $[O\text{ III}]\lambda 5007$, $[N\text{ II}]\lambda 6583$, and $[S\text{ II}]\lambda\lambda 6716, 31$. All measurements are performed man-

ually using the SPLOT routine of IRAF². Line intensities and equivalent widths are measured integrating all the emission between the limits of the line and over a local adjacent continuum. However, because of the faintness of many of the detected emission lines, a detailed inspection of the spectra is always necessary to get a proper estimation of the adjacent continuum and the line flux in these cases. For each emission line (in particular, for the hydrogen Balmer lines, as they are affected by absorptions of the stellar component of the galaxy) we consider several measurements at slightly different continuum levels. For each spectrum, we choose the emission line fluxes which provide the best match and minimize the uncertainties of the derived properties (reddening coefficient and oxygen abundance). Uncertainties in the line fluxes were estimated for each line considering both the *rms* of the continuum and the width of each emission line. We require galaxies to have lines of $H\alpha$, $H\beta$, and $[N\text{ II}]\lambda 6583$ detected at greater than 5σ . We constrain as well the other nebular lines that we make use of to be detected at greater than 3σ . With these cuts our sample reduces to 424 galaxies from SDSS and 23 from Union2.1 for a total of 447 galaxies to analyze (see Table 1 and redshift distribution on Figure 1).

We start by checking the nature of the ionization of the gas within our sample galaxy using the so-called diagnostic diagrams, as firstly proposed by Baldwin, Phillips & Terlevich (1981) and Veilleux & Osterbrock (1987). These diagrams are useful tools to distinguish between pure star-forming regions, Low-Ionization

² Image Reduction Analysis Facility, distributed by NOAO which is operated by AURA Inc., under cooperative agreement with NSF

Table 2. Derived properties from the oxygen abundances estimation for galaxies classified as Star Forming or Composite.

Object	Class	$c(H\beta)$	W_{abs}										$12 + \log(O/H)$	$T_e [O III]$	$\log \frac{O^{++}}{O^+}$	$12 + \log(N/H)$	$\log(N/O)$
			[Å]	P01	PT05	M13a	M13b	PP04a	PP04b	KK04T	KDN2O2	OH_FINAL					
5	SF	0.11 ± 0.06	1.0^a	8.47	8.75	8.58	8.57	8.69	8.82	8.82	8.82	8.76 \pm 0.04	5175	-0.48	8.03	-0.68 ± 0.03	
10	SF	0.36 ± 0.01	1.0 ± 0.1	8.10	8.22	8.22	8.27	8.32	8.27	8.28	8.26 \pm 0.05	11175	-0.3	6.66	-1.43 ± 0.03		
30	SF	0.85 ± 0.01	0.3 ± 0.1	8.26	8.55	8.52	8.54	8.65	8.71	8.73	8.68	8.66 \pm 0.03	6475	-0.7	7.7	-0.93 ± 0.03	
83	SF	0.15 ± 0.12	1.0^a	8.08	8.33	8.46	8.53	8.63	8.63	8.61	8.58 \pm 0.02	7425	-0.64	7.61	-0.92 ± 0.08		
128	SF	0.32 ± 0.02	1.0 ± 0.1	8.07	8.19	8.28	8.38	8.46	8.35	8.27	8.33 \pm 0.04	10625	-0.32	6.95	-1.23 ± 0.03		
133	SF	0.63 ± 0.05	1.0^a	8.32	8.70	8.61	8.52	8.63	8.82	8.81	8.77	8.75 \pm 0.04	5275	-0.66	7.91	-0.8 ± 0.03	
...																	

Note. — P01: Pilyugin (2001a,a) using R_{23} and P ; PT05: Pilyugin & Thuan (2005) using R_{23} and P ; M13a: Marino et al. (2013) using the $O3N2$ parameter; M13b: Marino et al. (2013) using the $N2$ parameter; PP04a: Pettini & Pagel (2004) using a linear fit to the $N2$ parameter; PP04b: Pettini & Pagel (2004) using the $O3N2$ parameter; KK04T: Kobulnicky & Kewley (2004) using R_{23} and the ionization parameter defined in that paper, $q_{K,K04}$; KDN2O2: Kewley & Dopita (2002) using the $N2O2$ parameter (calibration only valid for objects in the high metallicity).

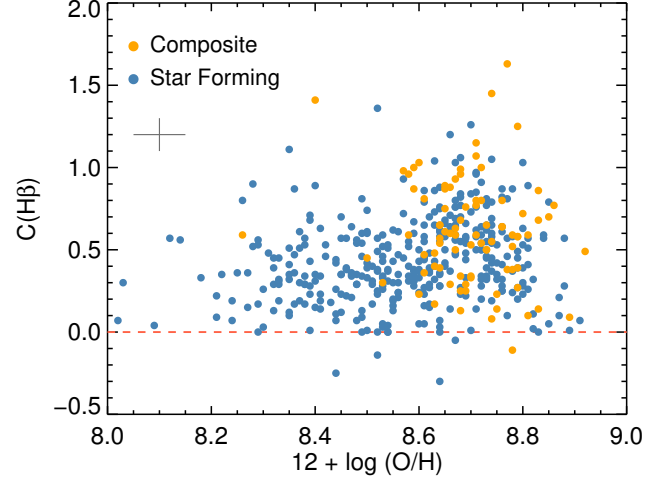


Figure 3. Reddening coefficient $c(H\beta)$. Galaxies with composite AGN/star-forming nature are plotted in yellow, and pure star-forming galaxies in blue. The coefficient $c(H\beta)$ obtained from the ratio $I(H\alpha)/I(H\beta)$ as a function of the oxygen abundance as $12 + \log(O/H)$. The (red) short-dashed line represents the no-reddening line ($c(H\beta) = 0$).

of H II Balmer lines –e.g., $H\gamma/H\beta$ or $H\delta/H\beta$ – can be measured too and the reddening coefficient can be determined with higher accuracy (e.g., see López-Sánchez & Esteban 2009). However, in extragalactic objects, the fluxes of nebular Balmer lines are affected by the absorption produced by the underlying stellar population (mainly B and A stars). We here consider that the Balmer lines are indeed affected by underlying stellar absorptions, and have taken into account the absorption in the hydrogen lines, W_{abs} –which we assume is the same for all the Balmer lines– following:

$$c(H\beta) = \frac{1}{f(\lambda)} \log \left[\frac{\frac{I(\lambda)}{I(H\beta)} \times \left(1 + \frac{W_{abs}}{W_{H\beta}}\right)}{\frac{F(\lambda)}{F(H\beta)} \times \left(1 + \frac{W_{abs}}{W_\lambda}\right)} \right], \quad (2)$$

as introduced by Mazzarella & Boroson (1993), where W_{abs} , W_λ , and $W_{H\beta}$ are the equivalent widths of the underlying stellar absorption, the considered Balmer line, and $H\beta$, respectively.

For some galaxies we are able to observe three H I Balmer lines ($H\alpha$, $H\beta$, and $H\gamma$). Hence, we derive the best $c(H\beta)$ and W_{abs} that match the observed fluxes and equivalent widths. In the cases where only two Balmer lines (i.e., $H\alpha$ and $H\beta$) are detected, we assume $W_{abs}=1.0$ Å and derive the reddening coefficient using only the $H\alpha/H\beta$ ratio.

Typical analyses of star-forming galaxies usually consider that the theoretical $I(H\alpha)/I(H\beta)$ intensity ratio is 2.86, following the case B recombination for an electron density of $n_e=100 \text{ cm}^{-2}$ and electron temperature of $T_e=10000 \text{ K}$. However, the theoretical H I Balmer ratios have a dependence on the electron temperature –see Storey & Hummer (1995) and also Appendix A in López-Sánchez et al. (2015) –. Actually, this value of 2.86 changes to $I(H\alpha)/I(H\beta)=3.01$ for $T_e \sim 5000 \text{ K}$ (and reduces for higher T_e values). The values of these ratios are, in turn, related to the metallicity of the ionized gas, in the sense that objects with low (high) electron temperature have high (low)

oxygen abundance. We use the prescriptions given by López-Sánchez et al. (2015) –see their Appendix A– to consider the dependence of the theoretical H I Balmer line ratios on the electronic temperature, assuming the best value to the oxygen abundance provided by the empirical calibrations (see next subsection).

Once we determine the reddening coefficient, we correct all the emission lines we measure by using Eq. 1. The resulting line intensities are given in Table 1, (given in electronic format, we give here a portion as example), which lists for each galaxy (named with the supernova Ia hosted by the galaxy) in column 1, the nature of the emission as a symbol C, SF or A for composite, star-forming or AGN, respectively, in column 2, the corrected emission line intensities as $\frac{[\text{O III}]\lambda 3727}{\text{H}\beta}$, $\frac{\text{H}\gamma}{\text{H}\beta}$, $\frac{[\text{O III}]\lambda 5007}{\text{H}\beta}$ and $\frac{\text{H}\alpha}{\text{H}\beta}$, in units of $I(\text{H}\beta) = 100$, with their errors, in columns 3 to 10. For each line the observed, $I(\lambda)$, and theoretical, corrected for reddening, intensities, $I_0(\lambda)$, are given. Moreover, the emission line intensities $\frac{[\text{N II}]\lambda 6583}{\text{H}\alpha}$, $\frac{[\text{S II}]\lambda 6716}{\text{H}\alpha}$, and $\frac{[\text{S II}]\lambda 6731}{\text{H}\alpha}$ in units of $I(\text{H}\alpha) = 100$, with their errors, are given in columns 11 to 13. The equivalent widths in Å for H α , H β , and H γ emission lines are in columns 14 to 16, respectively. Colons indicate measurements with an uncertainty larger than 40%, including their uncertainties.

Figure 3 shows the reddening coefficient $c(\text{H}\beta)$ that we obtain from the ratio $I(\text{H}\alpha)/I(\text{H}\beta)$ as a function of the final estimated oxygen abundance (see next section). The red dashed line indicates the case where no reddening appears. In most of the star-forming galaxies the reddening is smaller than 1.0 dex, with an average value of ~ 0.4 dex, while the composite objects show higher values reaching 1.5 dex in some cases. As seen in López-Sánchez & Esteban (2010), Figure 3 seems to show the trend that the reddening coefficient increases with the oxygen abundance. Table 2 compiles the $c(\text{H}\beta)$ and W_{abs} values –and their associated errors– derived for each galaxy. (see next section for details about the table).

3.3 Chemical Abundances

3.3.1 Empirical Methods to estimate abundances

When the faint auroral lines, such as $[\text{O III}]\lambda 4363$ or $[\text{N II}]\lambda 5755$, are not detectable, the so-called strong emission line (SEL) methods should be used to estimate the chemical abundances of the ionized gas within the observed galaxy. The majority of the empirical calibrations rely on ratios between bright emission lines, which are defined by

the following parameters:

$$R_3 = \frac{I([\text{O III}]\lambda 4959) + I([\text{O III}]\lambda 5007)}{\text{H}\beta}, \quad (3)$$

$$R_2 = \frac{I([\text{O II}]\lambda\lambda 3727, 9)}{\text{H}\beta}, \quad (4)$$

$$R_{23} = R_3 + R_2, \quad (5)$$

$$P = \frac{R_3}{R_{23}}, \quad (6)$$

$$y = \log \frac{R_3}{R_2} = \log \frac{1}{P^{-1} - 1}, \quad (7)$$

$$N2 = \log \frac{I([\text{N II}]\lambda 6584)}{\text{H}\alpha}, \quad (8)$$

$$O3N2 = \log \frac{I([\text{O III}]\lambda 5007)}{I([\text{N II}]\lambda 6584)}, \quad (9)$$

$$N2O2 = \log \frac{I([\text{N II}]\lambda 6584)}{I([\text{O II}]\lambda\lambda 3727, 9)} \quad (10)$$

Reviews of the most-common empirical calibrations and their limitations can be found in Kewley & Ellison (2008), López-Sánchez & Esteban (2010) and López-Sánchez et al. (2012).

Two important issues must be considered when using the SEL technique: 1) To accurately compute some of these parameters (e.g., R_{23} , $N2O2$), the emission line fluxes must be corrected for reddening. Hence, this is providing an extra uncertainty of the results; 2) As the intensity of oxygen (or any other heavy element) lines do not monotonically increase with metallicity, some parameters, e.g., R_{23} , are actually bi-evaluated. Thus, for the R_{23} index the calibrations must be given for $12+\log(\text{O}/\text{H}) \lesssim 8.0$ (low metallicity) and $12+\log(\text{O}/\text{H}) \gtrsim 8.4$ (high metallicity). For these two reasons, it is very convenient –and lately it has been extensively used in the literature– to resort to parameters that monotonically vary with the oxygen abundance –i.e. parameters that are not bivaluated–, such as $N2$ or $O3N2$, which do not suffer the problems of the reddening correction nor of the bi-evaluation. Nevertheless, some caution has still to be taken using these parameters, as some biases still exist (more details in López-Sánchez et al. 2012, and references within). For example, $N2$ saturates at high metallicities ($12+\log(\text{O}/\text{H}) \gtrsim 8.65$), while $O3N2$ is not valid in the low-metallicity regime ($12+\log(\text{O}/\text{H}) \lesssim 8.1$).

3.3.2 Adopted oxygen abundances

SEL methods based on the Te method consider oxygen abundance data for which the direct measurement of the electron temperature – derived from line ratios such as $[\text{O III}]\lambda 4363/\lambda 5007$, see Osterbrock & Ferland (2006)– are available. On the other hand, calibrations based on photoionization methods use photoionization modelling to derive the oxygen abundance directly from emission line ratios.

We here use a combined approach to derive the oxygen abundance of our galaxy sample using several SEL methods. First, we use the empirical calibrations of Pettini & Pagel (2004, hereinafter PP04), which consider both the $N2$ and $O3N2$ parameters, to get a first estimation of the metallicity. This value is later used to constrain the theoretical H I Balmer lines according to the method explained in the previous section. Once the reddening correction is known, we derived the oxygen abundance using both the Pilyugin

(2001a,b) and Pilyugin & Thuan (2005, hereinafter P01 and PT05, respectively) calibrations – which are based on T_e and consider the R_{23} and P parameters –, and the Kobulnicky & Kewley (2004, hereinafter KK04) calibrations – which were derived following photoionization models and consider the R_{23} and y parameters. It is well established (e.g., López-Sánchez & Esteban 2010) that the SEL methods based on photoionization models overestimate the oxygen abundances given by the SEL based on the T_e method by 0.2–0.4 dex. Hence, we consider the relationship given by Lara-López, López-Sánchez & Hopkins (2013) to convert the derived KK04 values into T_e -based values. For the high-metallicity range $-12+\log(\text{O}/\text{H}) \geq 8.4$ – we also use the $N2O2$ –corrected for reddening– with the calibration provided by Kewley & Dopita (2002, hereinafter KDN2O2). We also use the Marino et al. (2013, hereinafter M13), based in $N2$ and in $O3N2$ parameters and, basically, an update of PP04 calibrations.

For the intermediate metallicity range, $8.0 \leq -12+\log(\text{O}/\text{H}) \leq 8.4$, we use an averaged value between the low- and high-metallicity relationships in all calibrations involving the R_{23} index. This averaged value is actually obtained weighting the equations considering the oxygen abundance provided by the PP04 method. The weighting factor was derived using a linear fit in the range $[0,1]$ between the high-end of the low-metallicity branch $-12+\log(\text{O}/\text{H})=8.0$ – and the low-end of the high-metallicity branch $-12+\log(\text{O}/\text{H})=8.4$ –. For example, if an object has $-12+\log(\text{O}/\text{H})=8.3$ following the $N2$ and $O3N2$ parameters, we assume that the oxygen abundance derived using equations involving R_{23} is 0.25 of the value of the low-metallicity equation and 0.75 of the value of the high-metallicity equation. The typical uncertainties of the oxygen abundances obtained following the SEL methods are 0.1 dex, which is the standard error used for SEL methods (see, i.e., López-Sánchez et al. 2012).

Following the above results, the adopted value for the oxygen abundance in each object is the averaged value of all the valid results, taking also into account that some calibrations are not valid in all the metallicity range (as it was said before, $N2$ is only valid for $-12+\log(\text{O}/\text{H}) \leq 8.65$, $O3N2$ can be only applied for $-12+\log(\text{O}/\text{H}) \geq 8.10$ and $N2O2$ is only valid for $-12+\log(\text{O}/\text{H}) \geq 8.40$). Moreover we have found that P01 and PT05 are not providing good results (see next subsection 3.3.3) and therefore we have not used them for the average calculation.

The results thus obtained are compiled in Table 2, where, for each galaxy, named by its SDSS-II SN identification number and the IAU name for Union2.1 SNe Ia, in column 1, the nature of the spectrum (only SF or C are included in the table) is in column 2, the reddening coefficient $c(H\beta)$ is in column 3, and the absorption equivalent width of $H\alpha$ is in column 4. Columns 5 to 12 give the oxygen abundance as $-12+\log(\text{O}/\text{H})$ as obtained from the above described empirical calibrations PP04 using $N2$ (called PP04a), PP04 using $O3N2$ (called PP04b), P01, PT05, KK04 once corrected for the T_e scale (called KK04T), the one from KDN2O2, and those from M13 (M13a from $O3N2$ and M13b from $N2$). Column 13 compiles the finally adopted oxygen abundance.

Once we obtain a value of the oxygen abundance using the SEL methods, and given the $[\text{O II}]/\text{H}\beta$ and $[\text{O III}]/\text{H}\beta$ ratios and the electron density, we used the five-level program for the analysis of emission-line nebulae included in IRAF

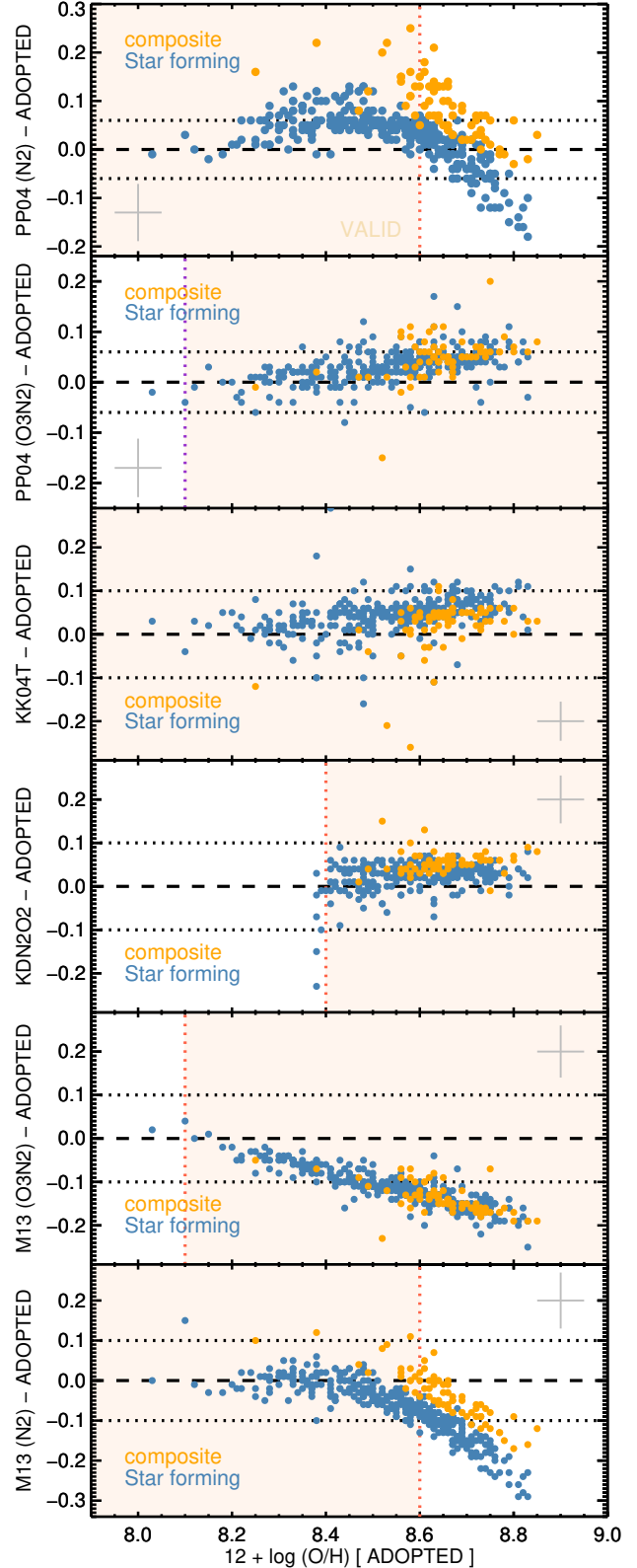


Figure 4. Comparing abundances. Blue circles are pure star-forming galaxies, while yellow circles represent galaxies with composite AGN/star-forming nature. Colored background represent the region where the measurement from each calibration is valid.

Table 3. Additional measured lines for the galaxies which we have determined the abundances by the direct method.

Object	Nature	T_e [O III]	T_e [O II]	$\frac{[\text{O III}] \lambda 4363}{H\beta}$		$\frac{[\text{O III}] \lambda 4959}{H\beta}$		$\frac{[\text{N II}] \lambda 6548}{H\beta}$	
				I	I_0	I	I_0	I	I_0
1119	C	9860 ± 980	9900 ± 680	3.72 ± 1.13	4.03 ± 1.23	217 ± 13	213 ± 14	82.4 ± 9.2	69.7 ± 7.8
3901	SF	9670 ± 1410	9770 ± 980	0.98 ± 0.42	1.11 ± 0.47	65 ± 3	64 ± 3	15.5 ± 2.6	11.9 ± 2.0
8719	SF	11050 ± 870	10730 ± 600	2.14 ± 0.47	2.39 ± 0.53	98 ± 3	95 ± 3	6.50 ± 0.7	5.1 ± 0.6
11172	SF	7940 ± 1150	8560 ± 800	0.24 ± 0.12	0.26 ± 0.13	31 ± 1	31 ± 2	50.6 ± 5.6	43.8 ± 4.9
13072	SF	8970 ± 710	9280 ± 490	0.98 ± 0.27	1.15 ± 0.32	92 ± 1	90 ± 2	30.5 ± 1.8	21.8 ± 1.3
15132	SF	11350 ± 1320	10940 ± 920	2.26 ± 0.70	2.56 ± 0.79	91 ± 12	89 ± 12	1.8 ± 0.3	1.4 ± 0.2

Table 4. Direct abundances

Object	Nature	$12 + \log(O^+/H^+)$	$12 + \log(O^{++}/H^+)$	$12 + \log(O/H)$	$\log(O^{++}/O^+)$	icf (N ⁺)	$12 + \log(N^+/H^+)$	$12 + \log(N/H)$	$\log(N/O)$
1119	C	8.01 ± 0.14	8.38 ± 0.06	8.53 ± 0.06	0.36 ± 0.15	3.31 ± 0.80	7.46 ± 0.08	7.98 ± 0.13	-0.55 ± 0.02
3901	SF	8.24 ± 0.21	7.88 ± 0.09	8.40 ± 0.15	-0.36 ± 0.23	1.44 ± 0.23	6.95 ± 0.13	7.11 ± 0.15	-1.29 ± 0.03
8719	SF	7.97 ± 0.08	7.89 ± 0.03	8.23 ± 0.04	-0.08 ± 0.08	1.83 ± 0.15	6.41 ± 0.07	6.67 ± 0.08	-1.56 ± 0.01
11172	SF	8.42 ± 0.22	7.90 ± 0.11	8.54 ± 0.17	-0.52 ± 0.25	1.30 ± 0.17	7.34 ± 0.13	7.45 ± 0.14	-1.09 ± 0.03
13072	SF	8.14 ± 0.11	8.14 ± 0.05	8.44 ± 0.06	-0.00 ± 0.12	1.99 ± 0.28	7.18 ± 0.07	7.48 ± 0.09	-0.96 ± 0.01
15132	SF	8.11 ± 0.16	7.79 ± 0.06	8.28 ± 0.11	-0.31 ± 0.17	1.48 ± 0.19	6.61 ± 0.11	6.78 ± 0.12	-1.50 ± 0.02

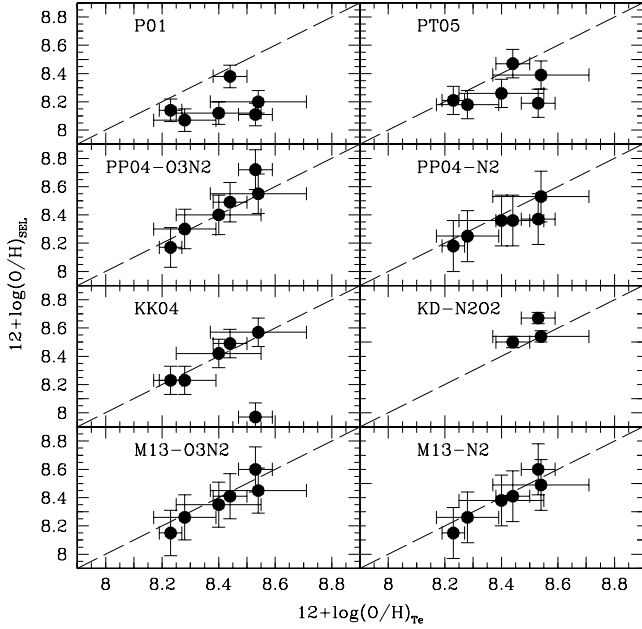


Figure 5. The comparison between the oxygen abundance obtained with the direct method for our six objects where it is possible to measure $[\text{O III}] \lambda 4363$ emission line and $12 + \log(\text{O}/\text{H})_{\text{Te}}$, with the one obtained with the different described SEL empirical calibrations, $12 + \log(\text{O}/\text{H})_{\text{SEL}}$, as labeled in each panel.

NEBULAR task³ (Shaw & Dufour 1995) to search for the T_e values that best reproduce the observations, also considering the relationship $T_e[\text{O II}] = 0.7 T_e[\text{O III}] + 3000$ (Garnett 1992). This exercise also provides an estimation of the ionization parameter, $\log(\text{O}^{++}/\text{O}^+)$, in each object. We also derive the nitrogen abundance, N/H , using the $[\text{N II}]/\text{H}\beta$ ratio and assuming the standard Peimbert & Costero (1969) ionization corrector factor (*icf*), $\text{N}^+/\text{O}^+ = \text{N}/\text{O}$.

Column 14 in Table 2 provides the high-ionization electronic temperature, $T[\text{O III}]$. Column 15 gives the $\log(\text{O}^{++}/\text{O}^+)$ ratio. Finally columns 16 and 17 provides the nitrogen abundances and the $\log(\text{N}/\text{O})$ ratio. The N/O ratio does not depend strongly on the electron temperature and hence we tabulate uncertainties for these values.

The errors of the adopted oxygen abundances consider the dispersion of the values derived following the valid methods, but it will never be inferior to the quadratic sum of the individual errors –e.g., if only 2 independent values are available, the error in the adopted oxygen abundance will not be inferior to $1/\sqrt{1/0.10^2 + 1/0.10^2} = 0.07$ dex–.

Figure 4 resumes the six calibrations we finally use, comparing for the whole sample each calibrated abundance with the adopted one. In the x-axis we have the adopted values while the y-axis represents the differences between each calibration and the adopted values. In each panel the limiting abundances for which the calibration is not longer valid is represented as a dotted line, while the identity or

³ We note that we used an updated atomic dataset for O^+ and S^+ for NEBULAR. The references are indicated in Table 4 of (García-Rojas et al. 2004).

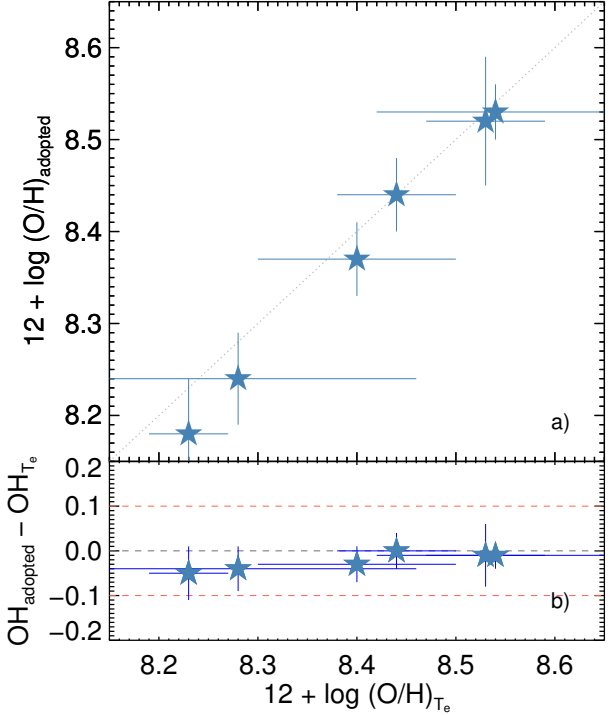


Figure 6. Differences between empirical and direct method abundances for the six galaxies for which this last one is possible. Top panel: the adopted abundance $12 + \log(\text{O}/\text{H})_{\text{adopted}}$ vs the direct method one $12 + \log(\text{O}/\text{H})_{\text{Te}}$. Bottom panel: The difference between both values as a function of $12 + \log(\text{O}/\text{H})_{\text{Te}}$.

zero value is the dashed line with dotted lines given the 1-sigma values. It is quite evident that using these limits, all the used calibrations are good.

Our final adopted oxygen abundances are shown in the left panel of Fig. 7 as a histogram. The solar value is marked with a long-dashed line. We have a small number of metal-poor galaxies, most of them have around solar metallicity. This bias comes from the SDSS data: small, metal-poor galaxies are not very common to find in their dataset, which is highly dominated by large galaxies, particularly at intermediate- and high-redshifts.

3.3.3 Comparison to the direct method (T_e)

We could detect the faint $[\text{O III}] \lambda 4363$ emission line in six galaxies. In those cases, therefore, we derive the oxygen abundance and the N/O ratio using the direct method, i.e., considering the electron temperature of the ionized gas. For this we use again the Shaw & Dufour (1995) five-level program included in IRAF NEBULAR task, first to derive $T_e[\text{O III}]$ and then to compute the ionic abundances, O^+/H^+ , O^{++}/H^+ and N^+/H^+ and the total O/H and N/O abundances. The N/O abundances were derived considering the *icf*(N^+) assumption given by Peimbert & Costero (1969).

Table 3 compiles the additional lines used in these spectra to measure the direct abundances. Column 1 shows the name of the SNe Ia, column 2 defines the nature of the galaxy (only SF and C are listed in this table). Columns

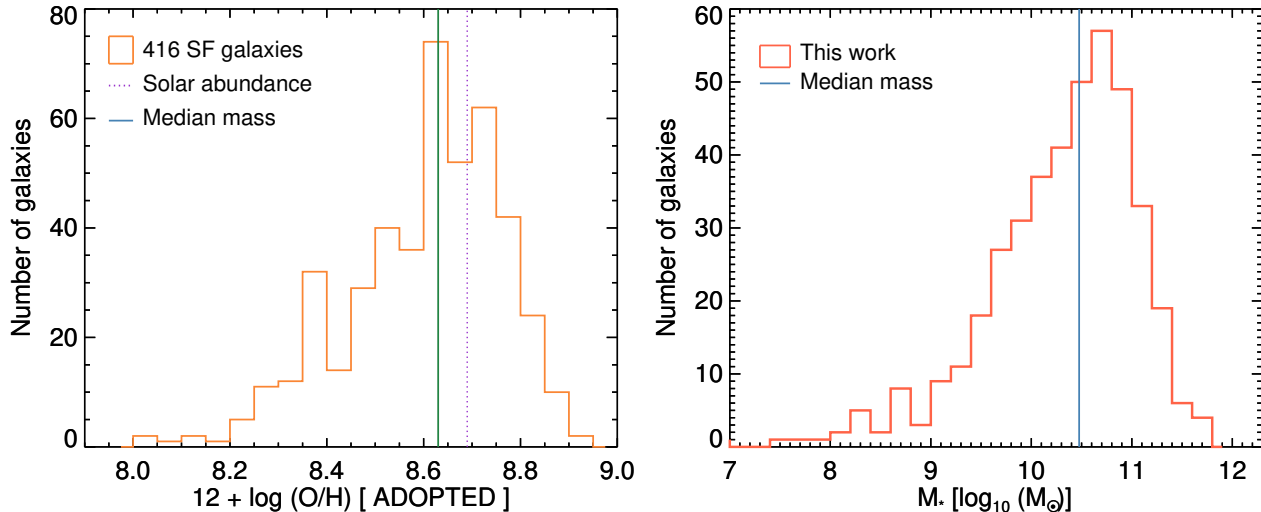


Figure 7. Distribution of determined abundances and stellar masses for the 416 galaxies with host galaxy properties available. In the left panel the solar value given by Asplund et al. (2009) is marked with a long-dashed line.

3 and 4 give electronic temperatures for high and low ionization zones, respectively. The additional emission line intensities as $\frac{[\text{O III}] \lambda 4363}{\text{H}\beta}$, $\frac{[\text{O III}] \lambda 4959}{\text{H}\beta}$ and $\frac{[\text{N II}] \lambda 6548}{\text{H}\beta}$, in units of $I(\text{H}\beta) = 100$, with their errors, in columns 5 to 10. For each line, the observed, $I(\lambda)$, and theoretical, corrected for reddening, intensities, $I_0(\lambda)$, are shown. Table 4 shows the direct abundances determined for these six galaxies.

Figure 5 shows the comparison of the direct method results with those obtained with each one of the calibrations described before. We see that, for these six galaxies, the results provided by the SEL techniques proposed by PP04 (both equations considering the N2 and the O3N2 parameters, respectively), KK04T (using the R23 and y parameters), KDN2O2 (using N2O2 parameter), and M13 (considering the O3N2 and N2 parameters, too), are valid to reproduce the direct method abundances, while the ones from P01 and PT05 are not good enough.

As the two top panels in Fig. 5 show, both P01 and PT05 are providing results that are typically 0.1 – 0.2 dex larger than the average value of the other SEL methods. This was a somewhat surprised result, as previous studies –e.g. López-Sánchez & Esteban (2010)– reported that P01 and PT05 were actually providing better results than the other SEL methods when compared to their Te-based oxygen abundances. We suspect that the reason of this behavior is consequence of our SDSS galaxy sample being very different to the galaxy sample whose H II regions were used to obtain the P01 and PT05 calibrations, introducing an additional important bias when deriving their oxygen abundances (see Stasińska 2010, for an extended discussion).

Therefore, we adopt for the oxygen abundance of each galaxy the averaged value of all the valid results, taking also into account that some SEL calibrations can not be used in all the metallicity range, since, as we said before, N2 is only valid for $12 + \log(\text{O}/\text{H}) \leq 8.65$, O3N2 can be only applied for $12 + \log(\text{O}/\text{H}) > 8.10$ and N2O2 is only valid for $12 + \log(\text{O}/\text{H}) > 8.40$.

Figure 6 shows the differences between the final adopted abundances and those from the direct method. It is clear

Table 5. Number of SNe/galaxies remaining after each step.

Step	SDSS	Union2.1	Total
Initial	1466	580	2046
Spectra in DR12	1128	60	1188
Emission line cuts	424	23	447
SF ionization	397	19	416
LC quality cuts	327	19	346
stretch/color cuts	245	18	263

that our method is good enough to obtain abundances as the ones estimated with the electronic temperature from the $[\text{O III}] \lambda 4363$ emission line. Therefore, we adopt this same criterion to estimate the oxygen abundances for the whole sample.

3.4 Stellar masses

We have estimated the stellar masses of our galaxies from their spectral energy distribution. For that we used STARLIGHT (Cid Fernandes et al. 2005; Mateus et al. 2006; Asari et al. 2007; Cid Fernandes et al. 2009), a program that fits a rest-frame galaxy spectrum (O_λ) in terms of a model (M_λ) built by a nonparametric linear combination of single stellar-population (SSP) spectra from a base spanning different ages and metallicities. The contribution of the different SSPs that best describe the original spectrum can be used to study the properties of the galaxy stellar populations and to estimate stellar velocity fields. In our case we have used the selection of the SSP model bases described in Stanishv et al. (2012) and already used in other works (e.g. Galbany et al. 2014, 2016a), which consists of 66 components with 17 different ages (from 1 Myr to 18 Gyr) and four metallicities ($Z = 0.2, 0.4, 1.0$ and $2.5 Z_\odot$, where $Z_\odot = 0.02$) coming from a slightly modified version of the models of Bruzual & Charlot (2003), replacing STELIB by the MILES spectral library (Sánchez-Blázquez et al. 2006),

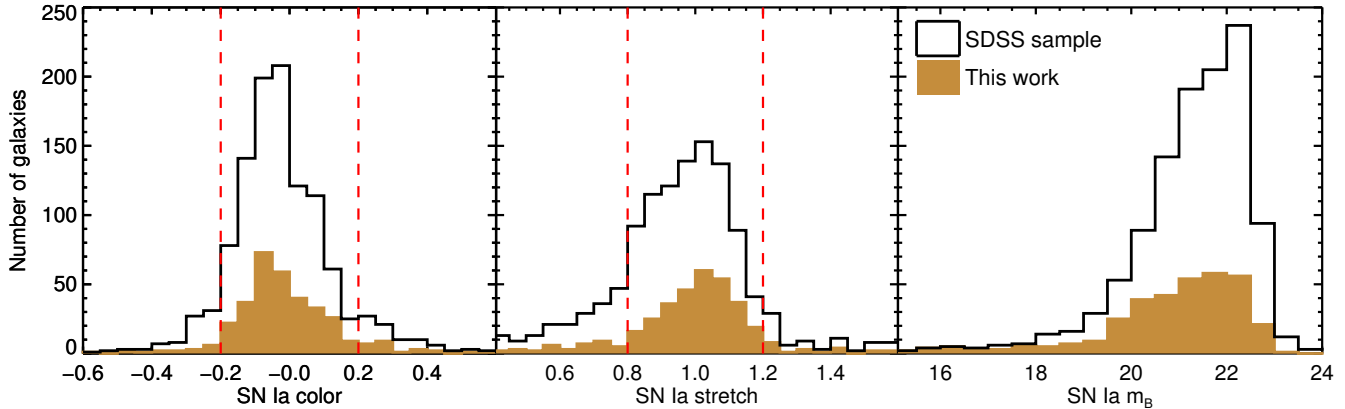


Figure 8. Properties of the SNe Ia SDSS sample and our host galaxy sample (golden shaded histograms). Left: Distribution of SNe Ia color, c . Center: SNe Ia stretch, s , distribution. Right: Distribution of apparent magnitudes, m_B . Red dashed lines define limits for color and stretch.

Table 6. SNe Ia LC parameters

Object	z	s	c	m_B	$\log[M_*/M_\odot]$	SNR
5	0.14195	1.03 ± 0.02	-0.08 ± 0.02	20.11 ± 0.03	10.714	5.7
10	0.05878	1.12 ± 0.04	0.76 ± 0.02	20.16 ± 0.03	8.408	3.9
30	0.14276	1.09 ± 0.02	-0.12 ± 0.01	19.51 ± 0.02	10.976	6.2
83	0.05025	0.98 ± 0.02	-0.1 ± 0.01	17.47 ± 0.02	10.132	5.5
128	0.15179	1.00 ± 0.02	-0.09 ± 0.02	20.04 ± 0.02	8.389	2.8
...						

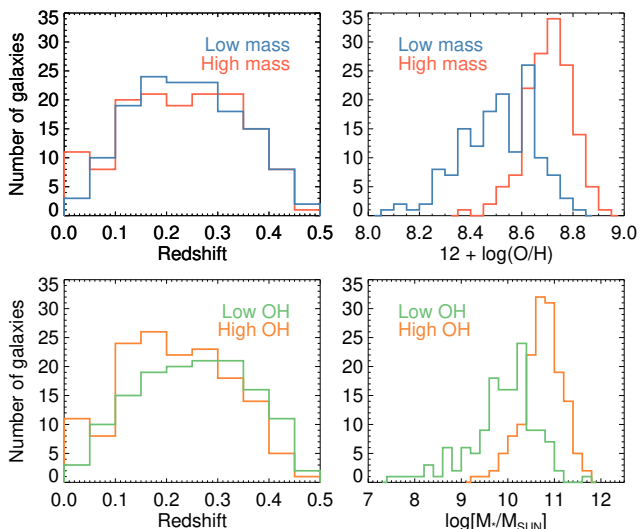


Figure 9. Distribution of our final sample of host galaxies. Left: distribution in redshift divided in two bins following the low and high stellar mass (top), or following the low and high oxygen abundances (bottom). Right: distribution in oxygen abundances with two stellar mass bins (top) and in stellar mass with two bins in metallicity (bottom), as labeled.

Padova 1994 evolutionary tracks, a Chabrier (2003) initial mass function (IMF) with lower and upper mass limits at 0.1 and $100 M_\odot$, respectively, and new calculations of the

TP-AGB evolutionary phase for stars of different mass and metallicity by Marigo & Girardi (2007) and Marigo et al. (2008). Dust effects are modeled as a foreground screen with a Cardelli, Clayton & Mathis (1989) reddening law with $R_V = 3.1$.

The output from STARLIGHT is the best contribution of SSPs of different ages and metallicities that reproduces the input spectrum. The total stellar mass is recovered by combining the mass-to-light ratio of the different SSPs contributing to the best fit. This stellar mass refers to the integrated star formation history and, therefore, includes stellar masses of different ages. A detailed analysis of the star formation histories of these galaxies will be presented elsewhere (Galbany et al. in prep.). The right panel of Figure 7, shows the distribution of these stellar masses for our sample of galaxies.

4 SN LC PARAMETERS

We fitted all SN Ia LCs with SiFTO (Conley et al. 2008) in order to obtain the apparent magnitude at peak (already corrected for Milky Way extinction), the width of the LC or stretch, s , and the SNe Ia color at maximum, c . SiFTO has been successfully used in several studies (Sullivan et al. 2010; Conley et al. 2011). We discarded SNe Ia that did not pass the following criteria in their LCs: 1) at least 4 points between -10 and 35 days from peak; 2) at least 2 points between -10 and 5 days from peak; 3) at least 1 point between $+5$ and $+20$ days from peak; and 4) at least 1 point between

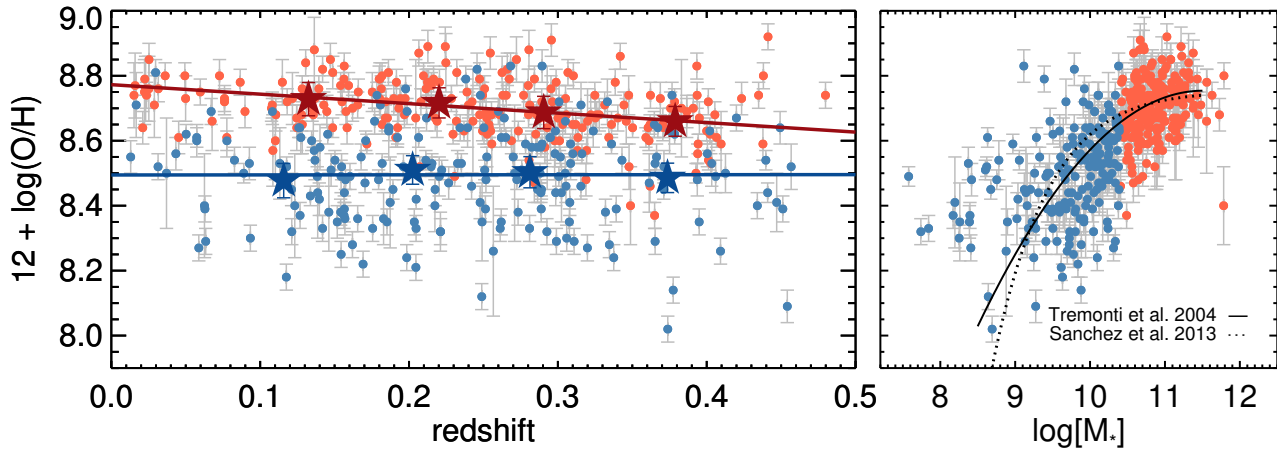


Figure 10. Left. The oxygen abundance as a function of the redshift. Right. The mass-metallicity relation. Red and blue points represent galaxies with stellar mass higher and lower than $\log M_* = 10.4$. Stars (red and blue) represent the abundances binned in four groups of similar sizes for each stellar mass set. The solid and dotted lines in the right panel are the fits found by Tremonti et al. (2004) and Sánchez et al. (2013), respectively.

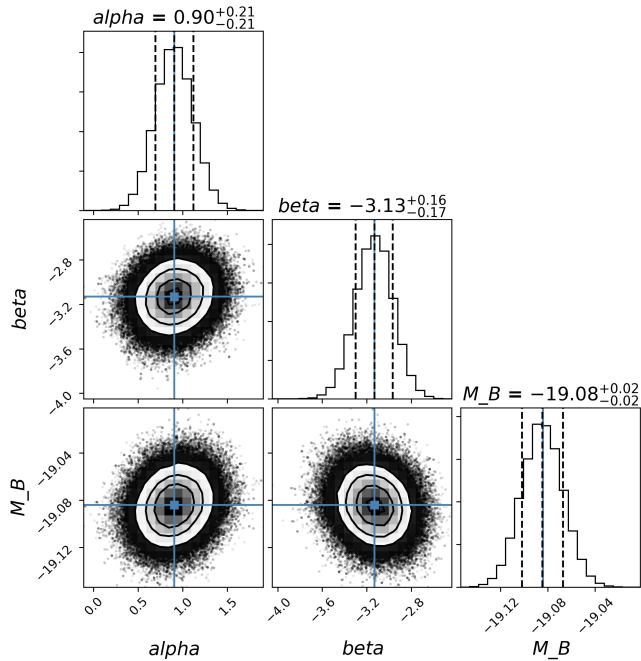


Figure 11. Corner plot of the posterior distributions for the three free parameters in our EMCEE fit (α , β , M_0).

-8 and +8 days from the peak in two different filters. From our 416 SNe Ia hosted in SF or C galaxies, 83% pass these quality cuts, the sample being now reduced to 346 objects. To the previous described quality cuts we have also applied cuts on color ($-0.2 < c < 0.2$) and stretch ($0.8 < s < 1.2$) pa-

rameters to keep a sample of SNe Ia as much similar as possible to a *normal* SN Ia. After this consideration, the number of remaining SNe Ia is 263.

Similarly to Fig. 7, Fig. 8 present the distributions of the SNe Ia LC parameters, color c , stretch s and apparent magnitude m_B and shows again no selection biases in our sample. We verify with this figure that our sample is not biased compared with the total SDSS sample.

Table 5 summarizes the number of SNe/galaxies useful for our analysis after each cut, and Table 6 lists redshift, light-curve parameters and host galaxy stellar mass for the remaining SN Ia in our final sample.

5 RESULTS AND DISCUSSION

5.1 Galaxy mass and metallicity distributions

We divided the sample into two groups according their mass and metallicity: galaxies are divided in two bins of low and high mass at $\log M_*/M_\odot = 10.4$. This limiting value is the median mass of our galaxy sample, in order to have the same size in both groups. Similarly the metallicity division is done at $12 + \log(\text{O}/\text{H}) = 8.64$ which is the median value of the oxygen abundance distributions (and almost the Solar value).

In Fig.9 we show the distributions in redshift, mass and metallicity of our subsamples as described above. Left panels show the redshift distributions divided by mass (top panel) and metallicity (bottom panel), which demonstrate that there is no bias on metallicity in our sample with redshift.

Right panels show the mass and metallicity distributions divided into two bins according to the other corresponding parameter of metallicity and mass, respectively. Both of them show the effect of the mass-metallicity relation with more massive galaxies in the high metallicity extreme and no metal-rich galaxies below $\log(M_*) = 9.2$.

Now that we have all quantities well determined for

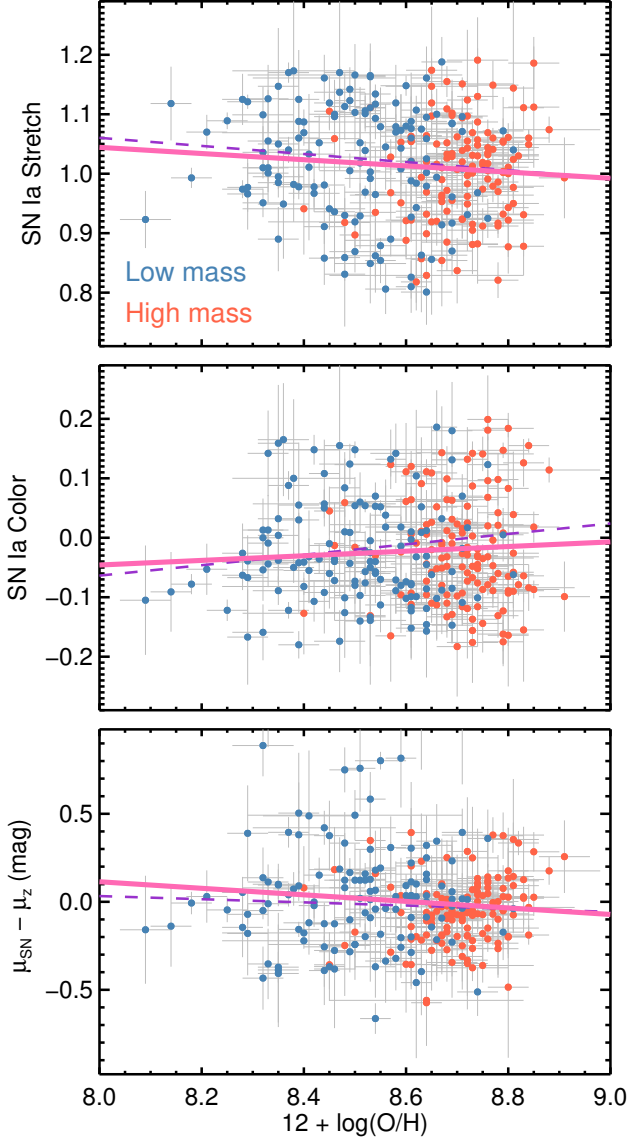


Figure 12. Dependences between stretch (top panel), color (middle panel), and Hubble residuals (bottom panel) oxygen abundance ($12 + \log(O/H)$ R) for our sample of SNe Ia .

SNe Ia and for their host galaxies, we are going to analyze the dependences among them, mainly to see if a correlation with the oxygen abundances appears.

5.2 Dependence of metallicity with redshift

In Fig. 10, left panel, we show the oxygen abundances we obtain with the method described in section 3.3.2 as a function of redshift. We perform least-squares straight lines for both bins, finding the following equations:

$$12 + \log(O/H)_{\text{hi-mass}} = -0.29(\pm 0.26) \times z + 8.77(\pm 0.07), \quad (11)$$

$$12 + \log(O/H)_{\text{lo-mass}} = 0.002(\pm 0.253) \times z + 8.49(\pm 0.06). \quad (12)$$

Low mass galaxies seem to show no variation of metallicity with redshift, but it is necessary to take into account that the dispersion is larger than in the massive galaxy group. Besides that, there is a possible selection effect that

would increase the number of massive/bright galaxies observed at higher redshift (Malmqvist bias effect). However, it is also true that these low stellar mass galaxies have usually stronger star formation rate (at least in this redshift range) and, therefore, the emission lines will be more intense, thus reducing, at least partially, the possible bias. On the other hand, we should emphasize that this figure does not have to be interpreted as an evolutionary scheme. Each galaxy has its own elemental abundance, but the evolutionary track of each galaxy may be completely different than the global trend shown by the whole sample. This finding would suggest that SNe in low-mass galaxies are possibly better standard candles, in line with findings by Rigault et al. (2013).

In the right panel we show the classical mass-metallicity relation found for our sample, and compare it to the relation found by Tremonti et al. (2004) using the full SDSS sample (scaled to the T_e abundance scale) and by Sánchez et al. (2013), for the local Universe ($0.005 < z < 0.03$). Our results are in agreement with both correlations, which is expected in the first case because we use spectra from the same SDSS sample, but also in the second case even though the redshift range of our galaxies is higher.

5.3 Hubble residual dependence on O/H

We construct a Hubble diagram from our SN light-curve measurements assuming a fixed standard flat Λ CDM cosmology with $H_0 = 70 \text{ km s}^{-1} \text{ Mpc}^{-1}$ and $\Omega_M = 0.295$ (Betoule et al. 2014). To this end, as a first step we minimized the likelihood function,

$$\ln(\mathcal{L}) = -\frac{1}{2} \sum_{\text{SN}} \left\{ \frac{[m_i^{\text{obs}} - m_i^{\text{model}}]^2}{\sigma_{\text{tot}}^2} + \ln(\sigma_{\text{tot}}^2) \right\}, \quad (13)$$

where m_i^{obs} is the apparent peak magnitude from SiFTO, and m_i^{model} is,

$$m_i^{\text{model}} = \mu^{\Lambda\text{CDM}}(z) + M_B - \alpha(s-1) + \beta c, \quad (14)$$

and the error budget contains the uncertainties of each term,

$$\sigma_{\text{tot}}^2 = \sigma_{m_i}^2 + (\alpha\sigma_s)^2 + (\beta\sigma_c)^2 + (\sigma_{\text{sys}})^2. \quad (15)$$

Due to our imperfect knowledge of SN Ia physics, commonly a σ_{sys} free parameter is included in the error budget to allow for further unaccounted magnitude variations. Given the nature of our minimization (we are fixing the cosmological parameters), σ_{sys} does not only account for intrinsic variations but for the fact that the assumed cosmological parameters have no errors.

Following de Jaeger et al. (2017), the best fit parameters from the minimization of the likelihood function are then used as a first guess to initialize a Bayesian Monte Carlo Markov Chain (MCMC) simulation using the Python-based package EMCEE (Foreman-Mackey et al. 2013). EMCEE uses an ensemble of walkers which can be moved in parallel to explore probability space, instead of a single iterative random walker (Goodman-Weare algorithm versus Metropolis-Hastings algorithm). Each walker attempts a specified number of steps, first proposing a new position, and then calculating the likelihood of the new position based on the data. The walker has a chance to move to the new position based on the ratio of the likelihood of its current position to that

Table 7. Least squares straight line fitting parameters: $y = ax + b$ for results of Fig. 12

Host parameter	SN parameter	intercept	slope	Significance	% slopes
POLYFIT	s	1.605 ± 0.080	-0.068 ± 0.009	7.35σ	—
	c	-0.765 ± 0.084	0.088 ± 0.010	8.96σ	—
	HR	0.751 ± 0.347	-0.090 ± 0.040	2.23σ	—
LINMIX	s	1.461 ± 0.326	-0.052 ± 0.038	1.38σ	91.6
	c	-0.357 ± 0.340	0.039 ± 0.039	0.99σ	84.3
	HR	1.600 ± 1.055	-0.186 ± 0.123	1.52σ	93.6

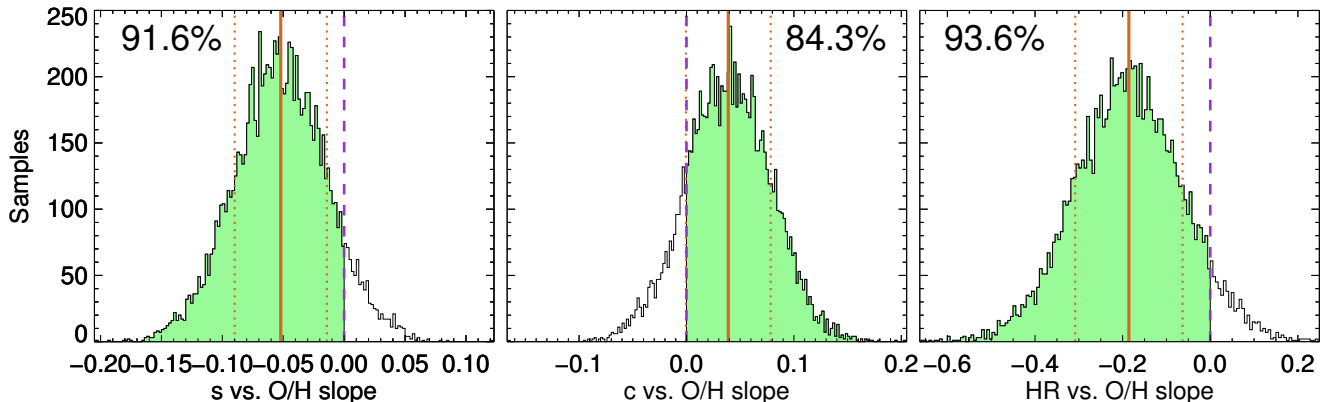


Figure 13. LINMIX posteriors for the slopes of the three fits shown in Figure 12. The percents correspond to the samples consistent with slopes different from zero and in the same direction of the average slope. All distributions are consistent with a Gaussian distribution, which is confirmed by the practically null difference between the mean and the median of each distribution.

of the new position. After a specified number of steps, the algorithm is completed and the position and likelihood of each walker as a function of step number is written out. These positions and likelihoods are used to generate the posterior probability distribution function for each model parameter. In our fit, we used 500 walkers and 1000 steps, although discarding the initial 100 steps to flatten the list of samples. Our prior probability distribution is defined to have flat probability for $0.0 < \alpha < 3.0$ and $1.0 < \beta < 6.0$ and $-21.0 < M_B < -17.0$ but otherwise have zero probability. We also attempted to use Gaussian priors, however no differences were found in the fit parameters. Following this procedure, in Figure 11 we show a corner plot with the parameter distributions from EMCEE, which gives the most probable values for M_B , α and β . We obtain the following mean values and standard deviations from the posterior distributions,

$$(M_B, \alpha, \beta) = (19.085 \pm 0.017, 0.905 \pm 0.213, 3.131 \pm 0.169). \tag{16}$$

Fig. 12 shows stretch, color, and HR, as a function of oxygen abundance, $12 + \log(O/H)$. All points are colored by the mass group they belong, which is divided by the median host galaxy stellar mass. To study possible correlations we use the LINMIX code, which is more robust than a simple linear fit because it takes into account the errors in both, x and y variables. This method computes a probability function for the data set, using a Markov Chain Monte Carlo (MCMC) algorithm. In each panel we show the best fit from LINMIX (thick pink solid line) together with a simple polynomial fit with the POLYFIT IDL library (thin dashed purple line). In Table 7 we give our results for the fitting param-

eters of the dependence of s , c and HR on oxygen abundance for both methods, and in Figure 13 we show the posterior distributions for the slopes given by LINMIX. Given that all distributions are consistent with Gaussians, we consider the significance of our relations statistically robust.

We find that the SNe Ia stretch s and color c show clear correlations with metallicity, independently of the method to fit the data, and in agreement with results from Childress et al. (2013) and Pan et al. (2014): metal-poor galaxies host higher stretch (narrower LCs) and with more negative colors (bluer) SNe Ia. On the other hand, the most interesting result is the correlation between the residuals of the HD and the oxygen abundance, with a significance of 1.52σ and a slope of $-0.186 \pm 0.123 \text{ mag dex}^{-1}$. In this sense, most metal-rich galaxies host slightly brighter SNe Ia *after standardization*, as other authors already reported (Johansson et al. 2013; Childress et al. 2013; Pan et al. 2014; Campbell, Fraser & Gilmore 2016; Wolf et al. 2016). This trend is in line with the difference in the Hubble residuals (step) between the two halves of the sample divided at the median value of the metallicity at 8.64 dex. We find that the metal-poor half of the sample has a positive HR of 0.080, while the metal-rich half has a negative HR = -0.026 (step of 0.106 mag). We compare our results with recent works from the literature in Fig. 14.

The slope obtained for HR vs $12 + \log(O/H)$, $-0.186 \text{ mag dex}^{-1}$, implies that SNe Ia located in metal-rich environments have smaller distance moduli than what it is expected for their redshift. In Paper I and II, we determined SN Ia absolute magnitudes by calculating distances to their

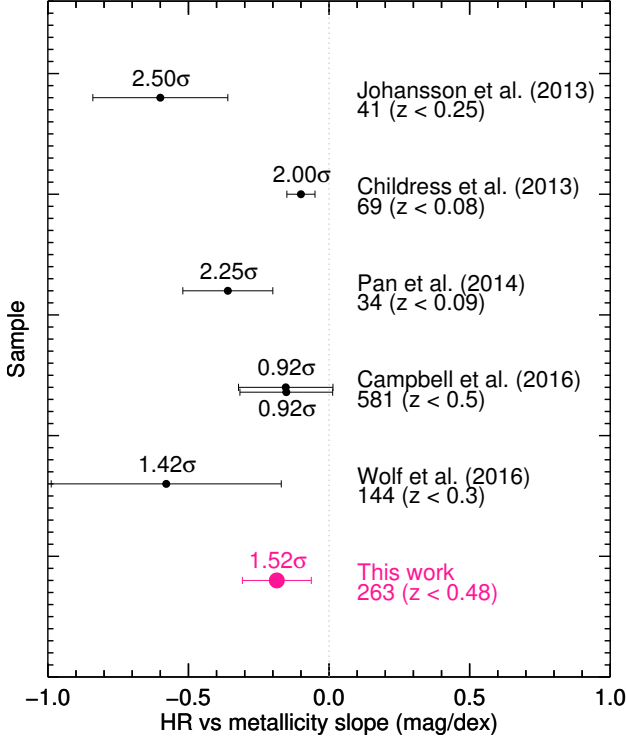


Figure 14. Comparison between our slope of the relationship HR vs the host galaxy oxygen abundance in mag dex^{-1} and others from the literature.

host galaxies using independent estimators (e.g. Cepheids & Tully-Fisher). We found a difference in this independent M_B measurement of 0.14 ± 0.10 mag between the metal-rich and metal-poor SNe Ia bins, which is in total agreement with the results found here. Moreover, this difference is also of the order of theoretical explosion models (~ 0.10 - 0.20 mag) from Bravo et al. (2010). However, all cosmological analyses, including this presented here, are still assuming a fixed M_B for all SNe Ia.

The way to solve this problem and obtain flat HR resides in adding a term in the standardization that includes this M_B dependence on metallicity. To this end, we repeated the EMCEE minimization but now adding a third parameter in our standardization model,

$$m_i^{\text{model}} = \mu^{\Lambda\text{CDM}}(z) + M_B - \alpha(s - 1) + \beta c - \gamma(OH - 8.64), \quad (17)$$

where 8.64 dex corresponds to the median oxygen abundance in our sample, and including the corresponding term in the total uncertainty budget,

$$\sigma_{\text{tot}}^2 = \sigma_{m_i}^2 + (\alpha\sigma_s)^2 + (\beta\sigma_c)^2 + (\gamma\sigma_{OH})^2 + (\sigma_{sys})^2. \quad (18)$$

The new best fit parameters determined from the posterior distributions are now,

$$(M_B, \alpha, \beta, \gamma) = (19.088 \pm 0.017, 0.932 \pm 0.214, 3.140 \pm 0.170, 0.160 \pm 0.113). \quad (19)$$

The change in M_B , α , and β is minimal, and we obtained a γ value compatible with being non-zero. We also confirmed

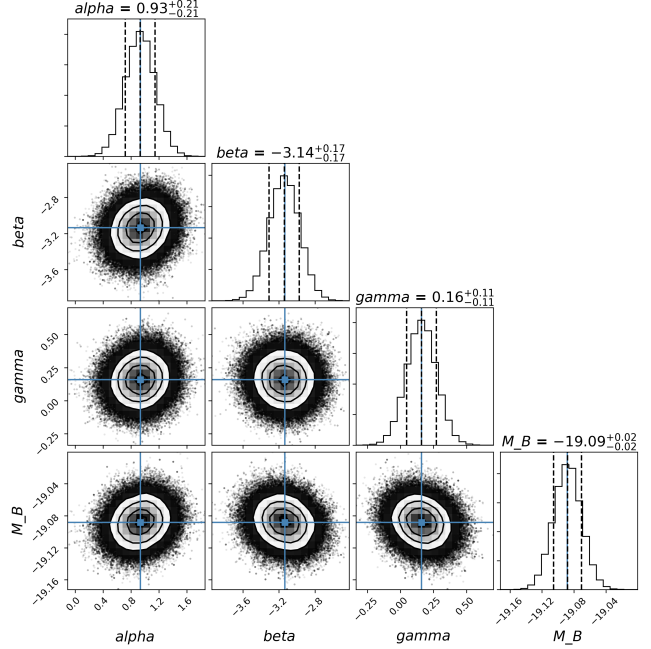


Figure 15. Similarly to Figure 11, corner plot of the EMCEE posterior distributions for our new model including the γ parameter which corrects for metallicity differences.

that using this new model the dependence with metallicity vanishes (slope posterior centered at zero).

6 CONCLUSIONS AND FUTURE WORK

Our project is divided in three parts: low, intermediate, and high redshift SNe Ia. After the analysis of a sample of SNe Ia in the local Universe (Paper I and II), here we presented the analysis performed to the intermediate redshift sample. Our conclusions are listed as follows:

- (i) We have estimated the oxygen abundances by carefully measuring the emission lines of a large sample of SN Ia host galaxies, for which the LC parameters and apparent magnitudes are available.
- (ii) We constructed a HD and fit the usual parameters M_B , α and β necessary to calculate the distance modulus for each SN Ia of our sample as: $\mu - (M_B + \alpha(s - 1) - \beta C)$. Our values are: $M_B = -19.085(\pm 0.017)$, $\alpha = 0.905(\pm 0.213)$ and $\beta = 3.131(\pm 0.169)$, in good agreement with results from other authors.
- (iii) The Hubble residual to a fixed ΛCDM cosmology shows a 1.52σ correlation with the global host galaxy oxygen abundance. The slope and significance of this correlation is similar to others given in the literature.
- (iv) The negative slope in the HR correlation with oxygen abundance is explained as fainter SNe Ia explode in metal-

richer environments, in the same way as we found in Paper I and II for the local Universe.

(v) We proposed the addition of a third parameter in the SN Ia standardization ($\gamma=0.160\pm0.113$), that accounts for the metallicity and corrects for the observed trend.

The main caveat of the addition of a third parameter in the standardization that accounts for the metallicity is that it will have a dependence on z , as we demonstrated in section 5.2, due to the chemical enrichment evolution of the Universe. In addition, and in contrast with our work at low- z in Paper I and II, we are here using metallicities measured from a fiber spectrograph that covers different fractions of the galaxy depending on its size and redshift. On average, galaxies have negative metallicity gradients, which translates in central regions having higher metallicities than outer regions (Sánchez et al. 2014). For this reason, fiber spectroscopy is known to suffer from aperture effects that have to be corrected for in order to obtain the *characteristic* metallicity of the galaxy (Iglesias-Páramo et al. 2013, 2016; Duarte Puertas et al. 2017).

More work is needed in this direction. On one hand, high-redshift SN Ia host galaxy spectroscopy in the near-infrared is needed to extend the Hubble diagram above 0.5. We have shown that higher-redshift galaxies are metal-poorer than nearby galaxies, so including those objects in an analysis similar to what we presented in this work would expand the dynamic range of abundances and therefore allow for steeper relations with Hubble residuals. In the third part of our project (see section 1) we will perform a similar analysis to that presented here but extending the redshift range beyond $z>0.5$, where differences among different cosmological models start to become evident, and also where the effect of the chemical enrichment evolution of the Universe may have a strong role.

On the other hand, performing local instead of global measurements of the oxygen abundance would be more reliable given that small- and large-scale galactic processes modify the abundance at different locations of galaxies. This effect would be more significant for those SNe Ia that explode further from the galaxy core. Fortunately, recent and future works would be able to provide such measurements through Integral Field Spectroscopy of galaxies at different redshifts (Galbany et al. 2016a).

ACKNOWLEDGEMENTS

This work has been supported by DGICYT/MINECO grants AYA2010-21887-C04-02 and AYA2013-47742-C4-4-P. M.E. M-R acknowledges financial support from the Ministerio de Economía y Competitividad (MINECO) through two grants for research visits to the Australian Astronomical Observatory (AAO) and to the Department of Astronomy of Universidad de Chile where this work was partially done. L.G. was supported in part by the US National Science Foundation under Grant AST-1311862. This work use Sloan Digital Sky Survey (SDSS) data. Funding for the SDSS and SDSS-II was provided by the Alfred P. Sloan Foundation, the Participating Institutions, the National Science Foundation, the U.S. Department of Energy, the National Aeronautics and Space Administration, the Japanese Monbukagakusho, the Max Planck Society, and the Higher Education Funding

Council for England. The SDSS was managed by the Astrophysical Research Consortium for the Participating Institutions. IRAF is distributed by NOAO which is operated by AURA Inc., under cooperative agreement with NSF.

REFERENCES

- Alam S. et al., 2015, ApJS, 219, 12
 Asari N. V., Cid Fernandes R., Stasińska G., Torres-Papaqui J. P., Mateus A., Sodré L., Schoenell W., Gomes J. M., 2007, MNRAS, 381, 263
 Asplund M., Grevesse N., Sauval A. J., Scott P., 2009, ARA&A, 47, 481
 Baldwin J. A., Phillips M. M., Terlevich R., 1981, PASP, 93, 5
 Barris B. J., Tonry J. L., 2004, ApJL, 613, L21
 Betoule M. et al., 2014, A&A, 568, A22
 Bravo E., Domínguez I., Badenes C., Piersanti L., Straniero O., 2010, ApJL, 711, L66
 Bruzual G., Charlot S., 2003, MNRAS, 344, 1000
 Burns C. R. et al., 2011, AJ, 141, 19
 Campbell H., Fraser M., Gilmore G., 2016, MNRAS, 457, 3470
 Cardelli J. A., Clayton G. C., Mathis J. S., 1989, ApJ, 345, 245
 Chabrier G., 2003, PASP, 115, 763
 Childress M. et al., 2013, ApJ, 770, 108
 Cid Fernandes R., Mateus A., Sodré L., Stasińska G., Gomes J. M., 2005, MNRAS, 358, 363
 Cid Fernandes R. et al., 2009, in Revista Mexicana de Astronomía y Astrofísica, vol. 27, Vol. 35, Revista Mexicana de Astronomía y Astrofísica Conference Series, pp. 127–132
 Conley A. et al., 2011, ApJS, 192, 1
 Conley A. et al., 2008, ApJ, 681, 482
 D’Andrea C. B. et al., 2011, ApJ, 743, 172
 Dawson K. S. et al., 2013, AJ, 145, 10
 de Jaeger T. et al., 2017, MNRAS, 472, 4233
 Duarte Puertas S., Vilchez J. M., Iglesias-Páramo J., Kehrig C., Pérez-Montero E., Rosales-Ortega F. F., 2017, A&A, 599, A71
 Foreman-Mackey D., Hogg D. W., Lang D., Goodman J., 2013, PASP, 125, 306
 Frieman J. A. et al., 2008, AJ, 135, 338
 Galbany L. et al., 2016a, MNRAS, 455, 4087
 Galbany L. et al., 2012, ApJ, 755, 125
 Galbany L. et al., 2014, A&A, 572, A38
 Galbany L. et al., 2016b, A&A, 591, A48
 Gallagher J. S., Garnavich P. M., Caldwell N., Kirshner R. P., Jha S. W., Li W., Ganeshalingam M., Filippenko A. V., 2008, ApJ, 685, 752
 García-Rojas J., Esteban C., Peimbert M., Rodríguez M., Ruiz M. T., Peimbert A., 2004, ApJS, 153, 501
 Garnett D. R., 1992, AJ, 103, 1330
 Gunn J. E. et al., 1998, AJ, 116, 3040
 Gunn J. E. et al., 2006, AJ, 131, 2332
 Gupta R. R. et al., 2011, ApJ, 740, 92
 Guy J. et al., 2007, A&A, 466, 11
 Guy J., Astier P., Nobili S., Regnault N., Pain R., 2005, A&A, 443, 781
 Henry R. B. C., Worthey G., 1999, PASP, 111, 919

- Hicken M. et al., 2009, *ApJ*, 700, 331
 Howell D. A. et al., 2009, *ApJ*, 691, 661
 Iglesias-Páramo J. et al., 2013, *A&A*, 553, L7
 Iglesias-Páramo J. et al., 2016, *ApJ*, 826, 71
 Jha S., Riess A. G., Kirshner R. P., 2007, *ApJ*, 659, 122
 Johansson J. et al., 2013, *MNRAS*, 435, 1680
 Kasen D., Röpke F. K., Woosley S. E., 2009, *Nature*, 460, 869
 Kauffmann G. et al., 2003, *MNRAS*, 346, 1055
 Kelly P. L., Hicken M., Burke D. L., Mandel K. S., Kirshner R. P., 2010, *ApJ*, 715, 743
 Kewley L. J., Dopita M. A., 2002, *ApJS*, 142, 35
 Kewley L. J., Dopita M. A., Sutherland R. S., Heisler C. A., Trevena J., 2001, *ApJ*, 556, 121
 Kewley L. J., Ellison S. L., 2008, *ApJ*, 681, 1183
 Kewley L. J., Groves B., Kauffmann G., Heckman T., 2006, *MNRAS*, 372, 961
 Kobulnicky H. A., Kewley L. J., 2004, *ApJ*, 617, 240
 Lampeitl H. et al., 2010, *ApJ*, 722, 566
 Lara-López M. A., López-Sánchez Á. R., Hopkins A. M., 2013, *ApJ*, 764, 178
 López-Sánchez Á. R., Dopita M. A., Kewley L. J., Zahid H. J., Nicholls D. C., Scharwächter J., 2012, *MNRAS*, 426, 2630
 López-Sánchez A. R., Esteban C., 2009, *A&A*, 508, 615
 López-Sánchez Á. R., Esteban C., 2010, *A&A*, 517, A85
 López-Sánchez Á. R., Westmeier T., Esteban C., Koribalski B. S., 2015, *MNRAS*, 450, 3381
 Maoz D., Mannucci F., Nelemans G., 2014, *ARA&A*, 52, 107
 Marigo P., Girardi L., 2007, *A&A*, 469, 239
 Marigo P., Girardi L., Bressan A., Groenewegen M. A. T., Silva L., Granato G. L., 2008, *A&A*, 482, 883
 Marino R. A. et al., 2013, *A&A*, 559, A114
 Mateus A., Sodr e L., Cid Fernandes R., Stasińska G., Schoenell W., Gomes J. M., 2006, *MNRAS*, 370, 721
 Mazzarella J. M., Boroson T. A., 1993, *ApJS*, 85, 27
 Mollá M., Díaz A. I., 2005, *MNRAS*, 358, 521
 Moreno-Raya M. E., López-Sánchez Á. R., Mollá M., Galbany L., Vílchez J. M., Carnero A., 2016a, *MNRAS*, 462, 1281
 Moreno-Raya M. E., Mollá M., López-Sánchez Á. R., Galbany L., Vílchez J. M., Carnero Rosell A., Domínguez I., 2016b, *ApJL*, 818, L19
 Nomoto K., Kobayashi C., Tominaga N., 2013, *ARA&A*, 51, 457
 Nordin J. et al., 2011, *ApJ*, 734, 42
 O'Donnell J. E., 1994, *ApJ*, 422, 158
 Osterbrock D. E., Ferland G. J., 2006, *Astrophysics of gaseous nebulae and active galactic nuclei*
 Pan Y.-C. et al., 2014, *MNRAS*, 438, 1391
 Peimbert M., Costero R., 1969, *Boletín de los Observatorios Tonantzintla y Tacubaya*, 5, 3
 Pérez-Montero E., Contini T., 2009, *MNRAS*, 398, 949
 Pettini M., Pagel B. E. J., 2004, *MNRAS*, 348, L59
 Phillips M. M., 1993, *ApJL*, 413, L105
 Phillips M. M., Lira P., Suntzeff N. B., Schommer R. A., Hamuy M., Maza J., 1999, *AJ*, 118, 1766
 Pilyugin L. S., 2001a, *A&A*, 369, 594
 Pilyugin L. S., 2001b, *A&A*, 374, 412
 Pilyugin L. S., Thuan T. X., 2005, *ApJ*, 631, 231
 Prieto J. L., Rest A., Suntzeff N. B., 2006, *ApJ*, 647, 501
 Riess A. G., Press W. H., Kirshner R. P., 1996, *ApJ*, 473, 88
 Rigault M. et al., 2013, *A&A*, 560, A66
 Sako M. et al., 2014, *ArXiv e-prints*
 Sánchez S. F. et al., 2014, *A&A*, 563, A49
 Sánchez S. F. et al., 2013, *A&A*, 554, A58
 Sánchez-Blázquez P. et al., 2006, *MNRAS*, 371, 703
 Schlafly E. F., Finkbeiner D. P., 2011, *ApJ*, 737, 103
 Scolnic D. M. et al., 2017, *ArXiv e-prints*
 Shaw R. A., Dufour R. J., 1995, *PASP*, 107, 896
 Stanishev V., Rodrigues M., Mourão A., Flores H., 2012, *A&A*, 545, A58
 Stasińska G., 2010, in *IAU Symposium, Vol. 262, Stellar Populations - Planning for the Next Decade*, Bruzual G. R., Charlot S., eds., pp. 93–96
 Storey P. J., Hummer D. G., 1995, *MNRAS*, 272, 41
 Stoughton C. et al., 2002, *AJ*, 123, 485
 Sullivan M. et al., 2010, *MNRAS*, 406, 782
 Sullivan M. et al., 2011, *ApJ*, 737, 102
 Sullivan M. et al., 2006, *ApJ*, 648, 868
 Suzuki N. et al., 2012, *ApJ*, 746, 85
 Thomas D. et al., 2013, *MNRAS*, 431, 1383
 Timmes F. X., Brown E. F., Truran J. W., 2003, *ApJL*, 590, L83
 Tremonti C. A. et al., 2004, *ApJ*, 613, 898
 Veilleux S., Osterbrock D. E., 1987, *ApJS*, 63, 295
 Wolf R. C. et al., 2016, *ApJ*, 821, 115
 York D. G. et al., 2000, *AJ*, 120, 1579